A&A 502, 665–678 (2009)
DOI: 10.1051/0004-6361/200911732

Astronomy & Astrophysics

The YOHKOH survey of partially occulted flares in hard X-rays

M. Tomczak

Astronomical Institute, University of Wrocław, ul. Kopernika 11, 51–622 Wrocław, Poland
e-mail: tomczak@astro.uni.wroc.pl

Received 27 January 2009 / Accepted 22 April 2009

ABSTRACT

Context. Modern solar X-ray imagers do not completely resolve the problem of deriving detailed diagnostics of faint hard X-ray sources in the presence of stronger ones. This is the case for the impulsive phase of solar flares in which footpoint sources are usually stronger than loop-top ones.
Aims. Flares that are partially occulted by the solar limb provide the most hopeful source of knowledge about hard X-ray loop-top sources. This work attempts to fill the gap between the published survey of partially occulted flares observed by RHESSI (Krucker & Lin 2008, ApJ, 673, 1181) and the extensive *Yohkoh* database.
Methods. Among the 1286 flares in the *Yohkoh* Hard X-ray Telescope Flare Catalogue (Sato et al. 2006, Sol. Phys., 236, 351), for which the hard X-ray images were presented, we identified 98 events that occurred behind the solar limb. We investigated their hard X-ray spectra and spatial structure.
Results. In most cases, we found that the hard X-ray spectrum of partially occulted flares consists of two components, non-thermal and thermal, which are cospatial to within 4 arcsec. For rest events, the components are separated, the non-thermal component clearly appearing to be situated higher. The photon energy spectra of the partially occulted flares are systematically steeper than spectra of the non-occulted flares. We can explain this difference as a consequence of intrinsically dissimilar conditions in coronal parts of flares, in comparison with the footpoints that usually dominate the hard X-ray emission of disk flares. At least two reasons for the difference should be taken into consideration: (1) stronger contamination of hard X-rays by emission from thermal plasma; and (2) different mechanisms in which non-thermal electrons radiate their energy. For events unbiased by the thermal component, the difference, $\Delta\gamma = \bar{\gamma}_{\rm LT} - \bar{\gamma}_{\rm FP}$, equals 1.5. We found a lack of correlation between the altitude of flares and the hard X-ray power-law index γ.
Conclusions. A schematic picture, in which a thin-target mechanism is responsible for the hard X-ray emission of loop-top sources and a thick-target mechanism for emission by footpoint sources, is modified by the presence of some coronal thick-target sources. Some of these sources exhibit evidence of magnetic trapping. For the characteristics of flares is conclusive the local magnetic configuration in which they occur.

Key words. Sun: corona – Sun: flares – Sun: particle emission – Sun: X-rays, gamma rays

1. Introduction

It has been commonly accepted that solar flares are caused by the reconnection of magnetic field lines in the corona. In this process, energy originally stored in the magnetic field is redistributed into plasma heating, wave generation, and particle acceleration. However, details of the reconnection process as well as general rules about energy partition are subjects of extensive debate. Any progress strongly depends on carefully planned observations and their interpretation.

Hard X-ray observations offer good insight into further evaluation of particles accelerated in the reconnection process. The propagation of particles operates under the guidance of the magnetic lines. Their bundles converge at the entrance into the lower part of the solar atmosphere, where the density of the ambient plasma increases steeply. Electrons accelerated in the corona are stopped there, emitting intense hard X-radiation via electron-ion bremsstrahlung. This mechanism, known as the thick-target model (Brown 1971), works so efficiently that footpoint hard X-ray sources usually strongly dominate the spatial distribution of flare emission in this energy range.

It is difficult to observe the particle acceleration without effects introduced by the propagation of particles because in the less-dense corona, hard X-radiation is emitted less efficiently in the thin-target model (Brown 1971; Lin 1974). In many cases, the coronal hard X-ray sources can be seen as the effect of magnetic convergence (Tomczak & Ciborski 2007) or ultra-dense thick-target environment (Kosugi et al. 1994; Veronig & Brown 2004).

Coronal hard X-ray sources can be easily distinguished when a flare occurs behind the solar limb but close enough to record emission from the higher part of the magnetic structure. In the case of a partially occulted flare, the solar disk works like a rough imager that stops the emission of usually brighter footpoint sources. Such a configuration had been used routinely for investigation of coronal hard X-ray sources before hard X-ray imaging detectors began to operate (Zirin et al. 1969; Frost & Dennis 1971; Hudson 1978; Hudson et al. 1982; Kane et al. 1982).

A first statistical attempt to analyze partially occulted flares was performed using data from the UCSD experiment onboard the *OSO-7* satellite (Roy & Datlowe 1975; McKenzie 1975). In fifteen months of *OSO-7* operation, from among 601 X-ray bursts above 10^3 photon cm^{-2} s^{-1} keV^{-1} in energy channel extending over 5.1–6.6 keV, 54 bursts were unaccompanied by Hα flares. Since a cinema flare patrol was in progress during those bursts, they probably occurred behind the solar limb.

From the group of partially occulted flares, McKenzie (1975) chose eight major soft X-ray events and found that all had significant hard X-ray emission in the 30–44 keV range. Roy & Datlowe (1975) analyzed all available hard X-ray spectra of partially occulted flares. They found that 25 of 37 bursts had a non-thermal component. The average value of the spectral indices at peak 20 keV flux for these 25 over-the-limb events was 4.6, whereas for 59 center events ($0° < \theta < 60°$) it was 3.8.

The main conclusion of the above mentioned papers from the pre-imaging era was that hard X-ray emission was not concentrated close to the solar surface but took place in extended regions in the corona.

Modern hard X-ray telescopes onboard the *Yohkoh* (Hard X-ray Telescope) and *Reuven Ramaty High-Energy Solar Spectroscopic Imager (RHESSI)* satellites have opened a new perspective in investigating coronal hard X-ray sources. Many important discoveries have been made (Krucker et al. 2008a) by including the most famous – the discovery of the presence of above the loop-top sources in flares (Masuda et al. 1994). However, in many cases the low dynamical range of a hard X-ray telescope creates problems for even a qualitative analysis of images, since detailed diagnostics of faint hard X-ray sources become difficult to measure in the presence of stronger ones. Alexander & Metcalf (1997) demonstrated that weak sources can be suppressed during the image reconstruction and mimic the appearance of stronger neighbors. This is indeed true for the impulsive phase of a typical flare when we observe strong footpoint and weak loop-top sources simultaneously.

To avoid this complication, partially occulted flares have been studied. From the *Yohkoh* database, one or a few examples of behind-the-limb flares have previously been selected many times. This specific configuration was usually used to derive joint diagnostics from hard and soft X-ray images by including full-Sun soft X-ray spectra recorded by the Bragg Crystal Spectrometer. In this way, soft X-ray bright loop-top kernels (Khan et al. 1995; Mariska et al. 1996; Sterling et al. 1996; Mariska & Doschek 1997; Ohyama & Shibata 1997) as well as flare-associated X-ray plasma ejections (Ohyama & Shibata 1997; Tomczak 2004, 2005) were investigated.

Mariska & McTiernan (1999) compared the hard and soft X-ray characteristics of 28 partially occulted and 17 non-occulted limb flares observed by *Yohkoh* between 1991 and 1996. For most observational characteristics, partially occulted flares were found to be indistinguishable from non-occulted ones. Exceptions were found for hard X-ray spectra averaged over entire events, which exhibited higher values of the power-law index γ in the partially occulted flares.

Tomczak (2001) investigated the *Yohkoh* X-ray images of 14 behind-the-limb flares. He reported their complex variability in hard X-ray flux which could be reproduced by two separate components: gradual lower-energy backgrounds lasting several minutes and quasi-periodic higher-energy impulses lasting typically 5–30 s. Impulses were too weak for imaging but gradual components enables an easy identification in hard X-ray images. The hard X-ray sources were usually cospatial with soft X-ray kernels, but sometimes had no distinct counterparts in soft X-rays. The appearance of a new gradual component in the hard X-ray light curve was always associated with the presence of an additional hard X-ray source.

Observations of the partially occulted flares were analyzed with *RHESSI* data (Krucker et al. 2007a; Li & Gan 2007; Liu et al. 2008), and either *Hinode* (Krucker et al. 2007b) or *Solar-Terrestrial Relations Observatory, STeReO* (Krucker et al. 2009) data. Krucker & Lin (2008) prepared a survey of partially occulted flares observed by *RHESSI*. They detected 55 of these events between 2002 February and 2004 August. Two different components of coronal hard X-ray emission were detected in 50 flares: (1) a thermal component with a gradual time profile; and (2) a non-thermal (power-law spectra with indices γ mostly between 4 and 7) component exhibiting more rapid time variations. Both components were usually cospatial within $\sim 2 \times 10^3$ km with only a few exceptions.

The interpretation of the extensive *Yohkoh* database would benefit from a survey of partially occulted flares, which this paper attempts to complete using the Hard X-ray Telescope Flare Catalogue. The development and structure of this catalogue are described in Sect. 2. The criteria of selection of flares enclosed in the survey are given in Sect. 3. In Sect. 4, a statistical approach to some characteristics describing partially occulted flares is given and the results are compared to their counterparts obtained for non-occulted flares from the catalogue. In Sect. 5, the results are discussed and compared to the reports of other authors. In Sect. 6, short descriptions of some interesting groups of events in the catalogue are given. Our main conclusions are summarized in Sect. 7.

2. Development and structure of the YOHKOH HXT Flare Catalogue

The Japanese solar satellite *Yohkoh* operated during the years 1991–2001 providing a huge amount of excellent data. The Hard X-ray Telescope, HXT, (Kosugi et al. 1991) was a Fourier synthesis imager observing the whole Sun. It consisted of 64 independent subcollimators measuring spatially modulated intensities in four energy bands (L: 14–23 keV, M1: 23–33 keV, M2: 33–53 keV, and H: 53–93 keV). During the flare, the intensities were integrated, in each energy band, over 0.5 s. Some reconstruction routines (Maximum Entropy Method, Pixons) that allow us to obtain hard X-ray images with an angular resolution of up to 5 arcsec are available.

Among the four scientific instruments onboard *Yohkoh*, the observations made by the HXT were organized in the most friendly way since the early years of the mission. The members of the HXT team prepared five versions of a catalogue by collecting basic information about flares observed by the telescope (see Table 1). The first two versions of the catalogue (Kosugi et al. 1993, 1995) contained 672 and 1007 records each. For some flares, the 10 min hard X-ray light curves in four energy bands were provided. In the 3rd version of the catalogue (Sato et al. 1998) containing 1264 records, example hard X-ray images were added. The last two versions of the catalogue contain the entire mission database with 3112 records and some supplementary data from other *Yohkoh* instruments. In the 4th version (Sato et al. 2003), the example soft X-ray images provided by the Soft X-ray Telescope (SXT) were introduced. In the 5th version (Sato et al. 2006), light curves and spectra provided by the Wide Band Spectrometer (WBS) were introduced.

In summary, the 5th version of the catalogue provides a short description of the 3090[1] flares that produced at least 3 counts s^{-1} per subcollimator (SC^{-1}) in channel L. The description contains date, time, peak counts in both four HXT and four WBS energy bands, *GOES* class, Hα position, and NOAA active region number. For 1286 flares, example images in particular energy

[1] Note that the total number of flares is slightly lower than the total number of records because more than one record is assigned to some flares.

Table 1. Development of the YOHKOH HXT Flare Catalogue.

Version	References	Latest event	Records	Contents				
				HXT (lc)[a]	HXT (i)[a]	*GOES*	SXT	WBS
1	Kosugi et al. (1993)	1992/12	672	+	–	+	–	–
2	Kosugi et al. (1995)	1994/12	1007	+	–	+	–	–
3	Sato et al. (1998)	1998/08	1264	+	+	+	–	–
4	Sato et al. (2003)	2001/12	3112	+	+	+	+	–
5	Sato et al. (2006)	2001/12	3112	+	+	+	+	+

[a] lc – light curves; i – images.

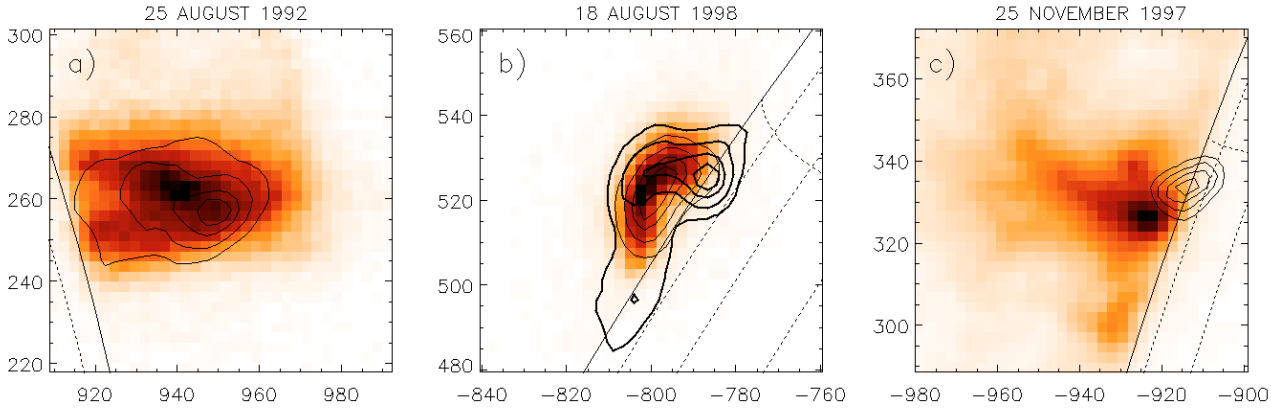

Fig. 1. Three examples of events that were considered during the preparation of the survey of partially occulted flares. Soft X-ray images (halftones) were obtained by the SXT in the Be119 filter, thin contours (10, 25, 50, and 75% of I_{max}) representing hard X-ray emission in energy band L (14–23 keV). Solid line shows solar limb and dashed lines represent heliospheric coordinates on the solar disk. **a)** Event included in the survey showing a typical coronal source. **b)** Event excluded from the survey because of footpoint sources seen in the energy band M2 (33–53 keV) – thick contours. **c)** Event included in the survey but excluded from statistical considerations due to possibly footpoint contamination (estimated longitude θ = E91.°6 ± 0.°6).

bands, basically for a peak time period, are enclosed. The criterion for inclusion of an image in the catalogue was a count rate of roughly 10 counts s^{-1} SC^{-1} above the background. The HXT images are superimposed on a SXT image when available. For the same 1286 flares four HXT light curves are presented. The catalogue also contains WBS light curves of 2736 flares. Example WBS spectra of 369 flares for energies up to 1 MeV and spectra of 12 flares for energies up to 10 MeV are added for a peak time period.

The last version of the catalogue still needs some improvements and corrections. For example, for the years 1997–2001 an identification of *GOES* class, Hα position, and NOAA active region number was made only for a minor part of events. The poor quality of some HXT images implies that their positions had been determined incorrectly, a conclusion that would agree with the observed disagreement with the Hα position of a flare.

3. Criteria of selection

In the first step, all hard X-ray images available in the catalogue were inspected. As a result, the preliminary list of 170 events, located close to the solar limb, was established. Each event from the preliminary list was then carefully verified using original files of data. For flares that occur behind the solar limb, the footpoint hard X-ray sources should not be detected. Therefore, every flare from the list, for which a centroid of any hard X-ray sources was located within the solar disk was rejected. If soft X-ray images of the flare were available, a decision about rejection was made by using these data. For flares that occur behind the solar limb, the solar limb appears to sharply intersect the soft X-ray emission. The counterparts of footpoint hard X-ray sources are also soft X-ray brightenings (Hudson et al. 1994; Tomczak 1997). Thus, for events in our survey, the soft X-ray brightenings should not be detected. If images of the flare taken during the time interval chosen in the catalogue did not allow us to decide, we used images for other time interval. Three examples of flares considered during the preparation of the survey are presented in Fig. 1.

Finally, we identified 98 flares that observations strongly suggested were behind the solar limb. The list of them is presented in Table 2. How far behind the solar limb are they located? The accurate knowledge of heliographic longitude, θ, is crucial to a correct measurement of altitude above the photosphere, h, one of the most important parameters in our discussion below. However, before the launch of the *STeReO* satellites, only a limited quality of estimation of the longitude was possible.

We estimate this parameter in two different ways. Our first method employed beyond-the-limb extrapolation of a straight line fitted to the plot of longitude versus time for all Hα flares observed in the proper active region during its passage across the solar disk (Roy & Datlowe 1975). In this approach, observations collected in the *Solar-Geophysical Data* (SGD) were used and an example of the longitude extrapolation for the flare No. 23 070 in the Catalogue from the NOAA AR 9087 is given in Fig. 2. In our second method we calculated the flare position on the basis of the time of central meridian passage (CMP) taken from the SGD for the proper active region. The formula describing the

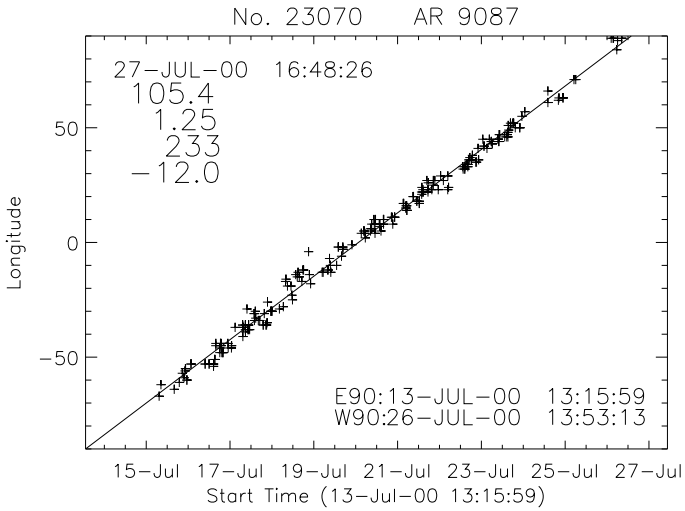

Fig. 2. Example of the longitude extrapolation. Description on the plot shows: time of event, value of θ and its uncertainty, number of points, average value of the latitude (*top*, *left*), and times of limb occurrences (*bottom*, *right*).

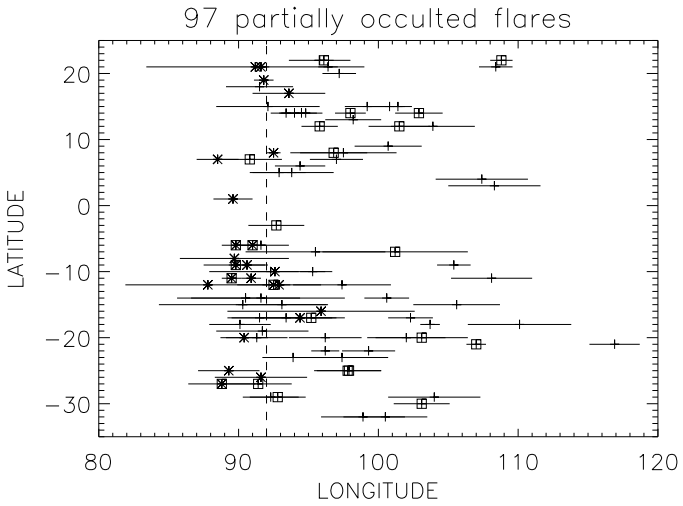

Fig. 3. Plot of heliographic coordinates (longitude versus latitude) for 97 flares from our survey. Events observed outside the maximum of hard X-rays are marked with boxes, events with possibly footpoint contamination are indicated by stars. The termination longitude for contamination (92°) is shown.

solar differentional rotation given by Newton & Nunn (1951) for large recurrent sunspots, corrected by Ward (1966), was used:

$$\theta = 13.45 - 3.0 \sin^2\phi \quad \mathrm{deg\,day^{-1}}, \tag{1}$$

where ϕ is the region latitude.

Both methods of estimating θ work well only for specific circumstances. The first shows the position of a weighted centroid of positions in which flares occurred in the active region during its passage across the solar disk. The second basically provides the position of the central part of an active region. Thus, if the investigated behind-the-limb flare occurred in an alternative place in the active region, each method may be affected some additional (systematic) error. This is why the derived values of θ were sometimes lower than 90°, although the available X-ray images provided strong indication that their positions beyond the solar limb were.

The values of θ given in Col. (6) of Table 2 were basically obtained by the first method, except for when the θ-t plot consisted of only a few points or the second method provided a more realistic solution. Uncertainties given in Col. (7) of Table 2 provide a measure of the scatter in the source data taken from the SGD. The results are summarized in Fig. 3, where the latitude is inferred directly from the hard X-ray image. The measured values of the longitude range between slightly below 90° (a consequence of systematic errors) and $26\overset{\circ}{.}9 \pm 1\overset{\circ}{.}8$ beyond the solar limb (event No. 26 060). For event No. 15 640 alone, we were unable to estimate the longitude.

At first glance, it seems that in our survey some partially occulted flares have been missed. We identified only 98 events out of 1286, i.e., 7.6% of the catalogue sources. Assuming a uniform distribution of flare longitude in the catalogue, one should expect that 4/22, i.e., 18.2% of the flares occurred behind the solar limb between 0° and 20°. We should recall, however, that the further the position of a flare beyond the solar limb, the larger is the occultation height. For 10°, hard X-ray emission should for example, occur at least about $\sim 1.1 \times 10^4$ km above the photosphere to be seen and for 20° the minimal height increases to about $\sim 4.6 \times 10^4$ km. This effect seriously decreases the population of partially occulted flares.

We estimated the corrected population of behind-the-limb flares by including the frequency of their occurrence in their dependence on the altitude, h, above the photosphere. We adopted the formula

$$\frac{\mathrm{d}N_h}{\mathrm{d}h} \sim \exp\left(-\frac{h}{h_0}\right) \tag{2}$$

where the scale-height $h_0 = (11 \pm 3) \times 10^3$ km was pointed out by Catalano & Van Allen (1973) for soft X-rays. The similar scale-height was inferred from the investigation of the peak time differences between the soft and hard X-ray emission of 859 flares (Li & Gan 2006). The obtained value (7.7±1.3)% agrees almost perfectly with the true population (7.6%) in the catalogue. We conclude that our survey is almost complete.

4. Results

We chose to characterize each event by its appearance during a single time interval given in the HXT Flare Catalogue. This time interval was chosen to contain the strongest hard X-ray signal. Its duration depended on both the number of counts and the imaging requirements, and was thus, sometimes only a few seconds around a single burst, and other times, many minutes with many bursts (see Cols. (3) and (14) in Table 2).

4.1. Power-law spectra

Within this time interval, the total signal above the background within the entire image was accumulated in each energy band, which meant that our results were unaffected by the disadvantages of imaging spectroscopy. We calculated flux ratios between consecutive energy bands: M1/L, M2/M1, and H/M2, the so-called hardness ratios. From the hardness ratios, the average power-law indices in some energy ranges of the hard X-ray spectrum were obtained: M1/L → γ1, between 14 and 33 keV; M2/M1 → γ2, between 23 and 53 keV; and H/M2 → γ3, between 33 and 93 keV.

Results are given in Cols. (11)–(13) of Table 2. Many events showed a signal above the background only for the low-energy bands, L and M1, thus for them there are no values of γ2 and γ3 in the table. For three flares, even the value of γ1 was not

Table 2. List of partially occulted flares found in the YOHKOH HXT Flare Catalogue[a].

(1)	(2)	(3)	(4)	(5)	(6)	(7)	(8)	(9)	(10)	(11)	(12)	(13)	(14)
00180	1991/10/21	12:51:00+38	C7.8	6891	S12E92.5	0.8	4.6	1.0	2.5	8.0	...	...	e, o, s
01050	1991/11/30	19:07:01+288	M1.0	6952	N21E108.4	1.2	34.4	1.0	42.0	9.4	...	...	m
01060	1991/12/02	04:53:11+76	M3.6	6952	N18E91.5	2.4	2.8	4.3	7.9	5.5	5.0	...	m
01320	1991/12/09	02:03:08+57	M1.4	6966	S06E91.0	1.0	1.9	2.0	3.7	9.5	...	...	e, o, s
01340	1991/12/09	04:19:09+242.5	M3.6	6966	S06E89.8	1.0	0	3.5	6.2	10.6	...	...	e, m, o
02270	1992/01/13	19:04:35+349.5	M1.3	7012	S10E95.3	0.9	10.1	4.9	11.8	9.9	...	...	m
02860	1992/02/06	20:51:22+240.5	M4.1	7030	N05W93.8	3.0	6.8	4.6	9.7	8.7	...	...	m
03270	1992/02/19	14:45:14+429	C9.4	7067	N06E94.4	1.8	8.4	3.0	7.4	8.5	...	...	m
04270	1992/06/28	04:47:05+153.5	X1.8	7205	N12W101.5	2.2	21.3	14.8	41.4	6.3	6.4	...	e, s
05090	1992/08/25	19:02:52+160	C8.7	7260	N13W98.2	2.0	15.2	14.1	32.7	8.5	...	...	s
05210	1992/09/06	09:20:11+27	C8.3	7276	N15E101.4	0.5	21.1	1.0	16.3	6.1	...	...	s
05260	1992/09/06	23:37:17+29	M1.3	7276	N17E93.6	2.6	6.4	1.0	3.2	8.3	7.5	...	o, s
05590	1992/10/05	09:24:28+47.5	M2.0	7293	S08W89.7	3.9	0	2.0	3.6	4.3	4.3	...	o, s
05920	1992/10/27	22:17:44+104.5	C5.4	7315	N07W88.5	1.5	0	4.1	7.5	7.6	...	...	m, o
06230	1992/11/01	11:44:06+53.5	C4.9	7321	S25W89.3	2.2	0	11.9	21.2	5.9	8.7	...	o, s
06240	1992/11/02	02:59:49+42	X9.0	7321	S25W97.9	2.3	14.2	14.6	33.6	8.0	7.3	6.0	e, g, s
06280	1992/11/05	20:30:17+167.5	C8.2	7323	S17W91.5	2.0	2.6	5.0	9.1	8.7	...	...	s
06440	1992/11/24	10:01:02+157	C6.9	7342	S07W95.5	5.0	7.4	3.0	8.6	6.5	...	...	s
06480	1992/11/24	20:31:03+271.5	C6.4	7342	S07W101.2	5.2	17.9	1.5	16.3	8.7	...	...	e, m
06810	1993/02/01	01:57:59+151	M2.2	7416	S10E92.6	1.7	4.6	1.0	2.5	6.9	4.6	...	m, o
06820	1993/02/01	06:58:25+119.5	M1.4	7416	S09E89.8	2.3	0.0	0.5	0.9	9.9	...	...	e, m, o
07580	1993/03/15	19:07:00+138.5	C5.5	7440	S06W91.6	2.0	3.0	3.5	6.5	7.5	...	...	m
07590	1993/03/15	21:05:53+479	M3.0	7440	S03W92.7	2.0	4.9	29.5	53.3	10.5	...	...	e, m
07680	1993/03/24	03:21:45+42	C6.6	7448	N15W92.1	3.7	3.8	2.7	5.3	6.2	7.4	...	s
08220	1993/06/24	14:54:48+176	C5.9	7530	S11E90.9	0.7	1.7	1.0	1.9	9.8	...	...	m, o
08230	1993/06/24	17:27:32+132.5	M4.2	7530	S11E89.5	0.7	0	4.6	8.2	10.8	...	...	e, s
08460	1993/09/26	10:26:04+63	C3.4	7590	N14E98.0	1.1	14.0	1.0	8.8	7.1	...	...	e, s
08470	1993/09/26	17:26:03+61	C3.4	7590	N14E94.0	1.1	7.0	1.0	3.5	7.6	...	...	s
08480	1993/09/26	18:29:18+54.5	C2.6	7590	N14E93.4	1.1	5.9	1.1	3.2	5.6	5.7	...	s
09650	1994/01/29	04:10:16+132	M2.4	7654	N05W92.9	1.9	5.2	3.0	6.2	...	...	...	c, s
09660	1994/01/29	11:24:49+80.5	M2.4	7654	N07W97.0	1.9	12.4	6.5	16.9	7.0	8.1	...	m
09700	1994/02/27	09:06:47+541	M2.8	7671	N08W97.5	3.8	13.6	12.6	38.6	7.9	...	...	h, m
11090	1997/11/25	05:34:45+162.5	C5.0	8113	N21E96.4	0.7	12.2	8.9	20.6	8.0	...	...	s
11100	1997/11/25	14:40:44+37.5	C1.1	8113	N21E91.6	0.6	3.1	0.5	1.2	5.6	...	...	o, s
11290	1998/01/03	17:13:25+127	M2.7	8124	S20W102.0	2.8	22.0	3.5	22.9	7.1	7.8	...	m
11510	1998/03/23	02:59:31+121.5	M2.3	8179	S22W99.3	1.9	16.6	15.7	38.3	8.4	...	...	s
11530	1998/03/24	01:47:46+60	C2.3	8180	S32W98.9	3.0	16.7	10.8	29.4	5.8	...	...	s
11540	1998/03/24	04:42:15+75	C4.3	8180	S32W100.5	3.0	19.7	10.0	32.0	6.3	...	...	s
11650	1998/04/23	05:39:55+151	X1.2	8210	S18E103.7	0.7	25.5	2.2	30.0	7.7	7.7	2.4	g, s
11660	1998/04/24	08:46:23+74.5	C8.9	8210	S20E91.3	2.2	2.3	13.5	24.2	4.7	5.1	...	s
11910	1998/05/08	14:20:54+67.5	M1.8	8210	S17W95.2	1.5	9.7	7.4	16.2	10.2	...	...	e, s
11930	1998/05/09	00:17:53+22.5	C8.3	8210	S14W100.6	1.6	19.7	1.1	14.4	6.3	...	...	s
11950	1998/05/09	03:22:56+70.5	M7.7	8210	S17W102.3	1.6	22.8	1.4	19.6	6.8	6.1	3.9	g, h, s
12000	1998/05/10	08:26:33+113	M1.6	8220	S27E91.4	2.4	2.6	4.5	8.2	9.8	...	...	e, s
12010	1998/05/10	13:18:30+14	M3.9	8220	S27E88.8	2.4	0	1.1	2.1	4.9	3.5	3.3	e, o, s
13580	1998/11/22	12:21:38+317.5	C8.8	8393	S17E93.4	4.2	6.2	3.0	6.6	8.8	...	...	m
13610	1998/11/23	05:58:41+39.5	C4.9	8384	S29W92.3	2.0	4.3	4.2	8.1	6.1	7.5	...	s
13620	1998/11/23	06:53:06+5.5	X2.2	8384	S29W92.8	2.0	5.2	8.3	15.7	10.3	...	...	e, s
13650	1998/11/24	02:17:48+316.5	X1.0	8384	S30W103.1	2.0	24.5	3.2	27.3	8.8	9.6	4.5	e, g, m
15640	1999/06/17	17:20:47+56.5	M3.6	8584	N22W??	...	>0	5.9	>10.5	7.7	...	...	e, s
16290	1999/07/23	05:01:27+44	C9.4	8645	S23E97.4	3.3	13.8	4.0	13.5	6.8	...	...	s
16310	1999/07/23	15:56:13+21.5	M1.0	8645	S26E91.6	3.3	3.0	1.1	2.3	5.5	6.5	...	o, s
16810	1999/08/07	19:13:10+309	M1.2	8645	S20W103.1	3.3	24.4	9.3	36.8	10.9	...	...	e, s
16820	1999/08/07	20:54:08+741	M1.7	8645	S29W104.0	3.3	26.1	3.9	31.5	10.0	...	...	m
17400	1999/10/01	00:15:28+60.5	C7.7	8716	N22E95.8	2.2	10.7	1.1	5.8	7.8	...	...	s
17710	1999/10/27	09:09:39+90.5	M1.0	8737	S12W87.8	5.9	0	1.8	3.2	6.0	4.4	...	o, s
17720	1999/10/27	13:28:21+535	M1.8	8737	S15W90.3	6.0	0.6	4.0	7.1	9.1	...	...	m

Table 2. continued.

(1)	(2)	(3)	(4)	(5)	(6)	(7)	(8)	(9)	(10)	(11)	(12)	(13)	(14)
17730	1999/10/27	15:28:00+762	M1.4	8737	S14W91.6	6.0	2.6	11.5	20.7	9.9	...	...	m
17790	1999/11/05	18:16:47+34	M3.0	8759	N12E95.8	1.3	11.0	7.0	16.2	8.4	...	...	e, s
18610	1999/12/17	00:19:22+74	C7.0	8806	N19E91.8	0.7	3.4	1.0	2.1	7.9	7.8	...	o, s
19030	2000/01/18	09:37:03+299	M1.2	8827	S15W105.6	3.1	28.2	1.8	30.9	6.8	7.0	...	m
19630	2000/03/07	03:48:58+24	C2.9	8906	S16E95.9	6.7	10.7	1.6	6.7	7.0	...	...	o, s
20920	2000/05/03	22:58:52+741	M1.1	8970	S18W90.1	2.2	0.0	7.4	13.2	9.3	...	...	m
20930	2000/05/05	15:18:42+1954	M1.5	8970	S18W110.1	3.7	37.5	2.2	51.6	8.5	4.7	...	m
20980	2000/05/12	08:41:48+85	C8.1	8998	S14E90.5	3.9	0.9	3.6	6.4	9.1	...	...	s
21030	2000/05/13	01:36:19+232	M1.1	9002	N22E108.8	0.8	33.8	4.9	51.5	9.5	...	...	e, s
21050	2000/05/14	00:25:08+97.5	C7.5	9002	N22E96.1	0.7	11.0	4.5	12.3	7.2	...	...	e, s
21280	2000/05/17	04:02:46+14	C7.1	8993	S20W90.4	1.7	0.7	2.0	3.6	4.6	5.0	...	o, s
21530	2000/05/24	03:13:26+83.5	C7.0	9017	S12E92.9	3.0	5.3	2.1	4.6	7.9	...	...	o, s
21880	2000/06/12	01:37:32+10	C6.1	9042	N21E91.2	7.8	2.2	1.6	3.0	5.8	4.1	...	o, s
22570	2000/07/15	04:33:29+32	C2.7	9090	N14E94.8	0.8	8.5	0.5	3.4	...	...	...	l, s
23070	2000/07/27	16:46:58+111	M1.5	9087	S09W105.4	1.2	26.9	5.7	36.7	7.2	8.4	...	s
23590	2000/09/22	23:46:52+69	C8.5	9165	N14W94.5	1.5	8.0	4.6	10.4	5.6	6.6	...	s
23750	2000/09/30	20:15:37+17.5	M1.8	9169	N07W90.8	2.3	1.4	3.6	6.5	9.2	...	...	e, s
23780	2000/10/01	07:01:39+26	M5.0	9169	N08W96.8	2.4	12.2	10.6	23.9	10.2	...	...	e, s
23790	2000/10/01	14:00:08+56	M2.2	9169	N09W100.7	2.4	19.2	2.1	16.3	6.0	6.6	...	m
23810	2000/10/02	02:17:44+23	C5.0	9182	N01E89.6	1.4	0	2.0	3.6	4.8	4.6	...	o, s
23940	2000/10/16	05:41:56+166	C7.0	9182	N04W107.4	3.3	30.1	3.0	39.0	7.1	9.6	...	m
23950	2000/10/16	06:59:48+1018.5	M2.5	9182	N03W108.3	3.3	31.5	4.0	44.6	10.8	...	...	s
24480	2000/12/08	16:18:57+90.5	C4.3	9246	S09W90.6	1.3	1.1	2.1	3.8	7.0	...	...	m, o
24580	2000/12/18	20:12:57+27	C2.7	9280	N08E92.5	0.5	4.4	2.0	4.2	9.3	...	...	o, s
24840	2001/01/03	18:05:31+44.5	C2.7	9302	N20E97.2	1.2	12.8	9.0	22.0	...	...	...	c, s
25540	2001/04/01	11:42:36+36	M5.5	9415	S21E107.0	0.7	30.3	23.6	77.9	9.2	6.7	...	e, h, s
25870	2001/04/05	02:06:55+75	M3.1	9393	N15W99.2	1.6	16.3	3.2	15.2	6.1	6.8	...	s
25880	2001/04/05	05:12:45+119	M1.1	9393	N15W100.8	1.6	19.3	4.6	21.3	8.1	...	...	m
25890	2001/04/05	08:33:08+8	M8.4	9393	N14W102.9	1.7	23.1	6.3	30.1	8.3	6.6	...	e, s
26060	2001/04/18	02:14:29+36.5	C2.2	9415	S21W116.9	1.8	47.9	9.0	108.4	3.4	3.7	3.7	g, s
26480	2001/05/20	06:02:17+6.5	M6.4	9455	S17W94.4	2.6	8.1	0.7	3.4	4.0	3.4	3.6	o, s
26490	2001/05/20	09:19:43+51.5	M1.5	9455	S20W96.2	2.6	11.3	1.0	6.1	8.5	5.8	...	m
27080	2001/08/09	00:39:15+120	C6.0	9557	S19W91.7	3.3	3.1	5.4	9.9	6.6	7.9	...	s
27400	2001/08/29	09:12:02+59.5	C6.5	9587	S12W97.4	3.5	12.7	1.0	7.8	6.7	8.3	...	s
27500	2001/09/03	01:54:38+133	C9.0	9607	S15E93.1	3.3	5.6	3.4	7.1	10.1	...	...	s
27540	2001/09/03	18:23:03+193.5	M2.5	9608	S22E96.2	1.0	12.2	1.4	6.9	8.1	6.9	...	m
27890	2001/09/11	07:00:00+69	M1.2	9616	S10E92.3	4.4	4.1	6.8	12.7	8.0	...	...	s
28260	2001/09/19	06:54:11+56.5	C7.2	9608	S23W93.9	2.2	7.6	10.2	19.9	5.6	7.2	...	s
29110	2001/10/29	01:56:00+41.5	M1.3	9669	N12W103.9	3.0	25.5	2.5	26.0	5.3	5.0	...	m
30430	2001/12/01	15:12:21+847	M4.8	9727	S25E97.8	2.4	14.3	13.6	31.6	9.0	...	...	e, m
30470	2001/12/02	21:29:50+251.5	M2.0	9714	S11W108.1	2.9	32.5	8.6	53.0	9.7	...	...	m

[a] Descriptions: (1) – catalogue event number; (2) – date (YYYY/MM/DD); (3) – time integration (start time [UT] + duration in seconds); (4) – GOES X-ray class; (5) – NOAA active region number; (6) – location in solar coordinates; (7) – uncertainty of longitude estimation; (8) – estimated number of hours before/after the limb passage; (9) – altitude of HXR centroid above the solar limb in SXT pixels [2.45 arcsec]; (10) – estimated total height in 10^3 km; (11) – $\gamma 1$, the power-law index from hardness ratio M1/L; (12) – $\gamma 2$, the power-law index from hardness ratio M2/M1; (13) – $\gamma 3$, the power-law index from hardness ratio H/M2; (14) – remarks: c – corrupted HXT file (no HXT diagnostics), e – maximum of flare outside the time integration, g – gamma rays, h – progressive spectral hardening, l – only channel L (no HXT diagnostics), m – multiple bursts, o – event situated too close to the solar limb, possibly footpoint contamination, s – single burst.

obtained: for two of them (Nos. 09 650 and 24 840) source data files were corrupted, and for event No. 22 570 the hard X-ray flux was recorded only in the channel L. Uncertainties in the γ indices, estimated according to the number of counts using the Poisson statistics, were typically 0.1–0.2.

In Fig. 3, two kinds of flares not included in our statistical analyses are marked. The events marked with boxes were not observed in the maximum of hard X-rays, and therefore values of γ indices obtained for them are unrepresentative of the highest energy phase available for other events. For uniformity of results, these flares are omitted in the later analysis.

The events marked in Fig. 3 with stars probably occurred too close to the solar limb and the possibility of hard X-ray emission from their footpoints is not excluded completely. For these events a small hard X-ray source is indeed seen centered close to the solar limb (e.g., Fig. 1c). Its size is much smaller than a size of a typical coronal source. We found that these sources are seen basically for the longitudes below 92°. Our aim is to study the characteristics of coronal hard X-ray sources, therefore these flares are also omitted in our later analysis.

A histogram of the $\gamma 1$ index values obtained for 94 events in our survey is presented in Fig. 4, where also superimpose two separate histograms, one for events without the hard X-ray maximum (boxes in Fig. 3) and another for events with possible footpoint contamination (stars in Fig. 3). With respect to our expectations, the first histogram, which contains the less energetic events, is shifted towards higher values, while the second, including more energetic events, is shifted towards lower values. We conclude that because of strict selection criteria applied, the final population is more uniform.

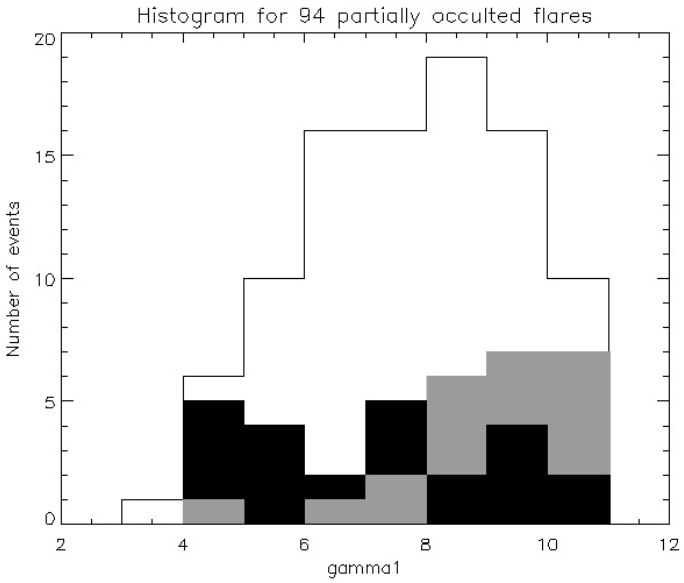

Fig. 4. Histogram of values of power-law index obtained for 94 partially occulted flares in energy range 14–33 keV. Gray bins represent 24 events that were not observed in the maximum of hard X-rays, black bins represent 24 events with possibly footpoint contamination.

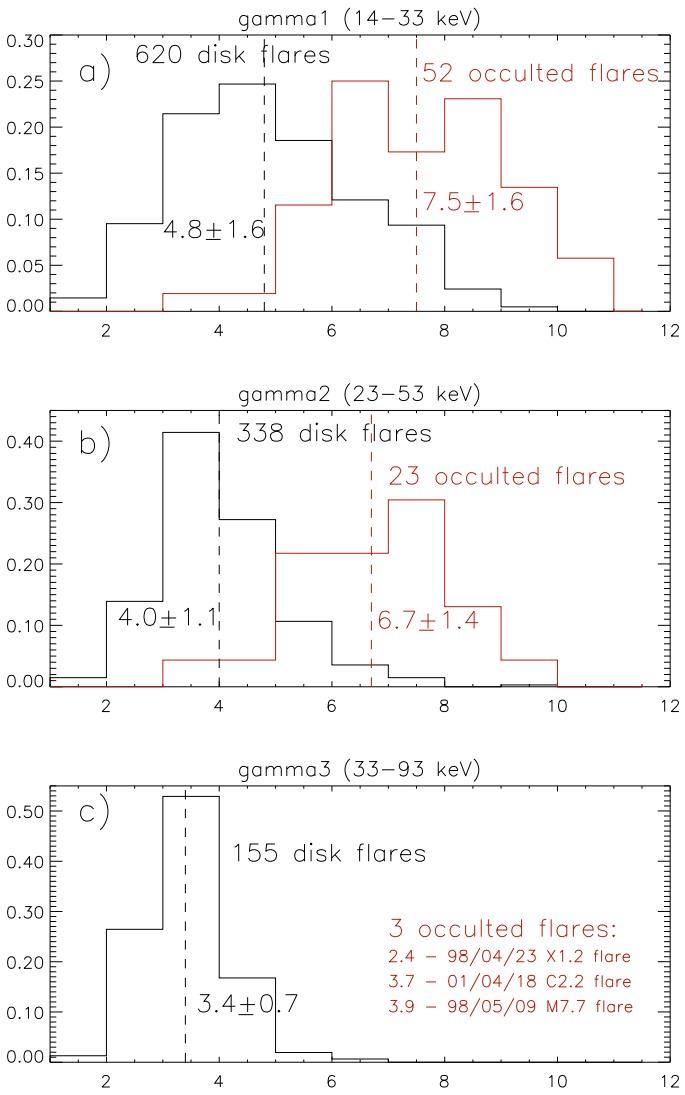

Fig. 5. Normalized histograms of values of the power-law index fitted in different ranges of the hard X-ray energy photon spectrum. Separate histograms for partially occulted and disk flares are presented. Energy ranges, number of events, average values and standard deviations are written.

We present the final histogram in Fig. 5a. It contains values for 52 partially occulted flares remaining after rejection of the two groups of events described in the previous paragraph. The histogram of values of the $\gamma 1$ index obtained for 620 non-occulted flares identified in the catalogue is given in the same panel. For straightforward comparison, both histograms are normalized. As we can see, the central parts of the histograms, containing about two third of events, are shifted with respect to each other. The average value for partially occulted flares is 7.5, while the average value for non-occulted flares is 4.8. Standard deviations for both histograms are 1.6.

In Fig. 5b, we compare normalized histograms of the $\gamma 2$ index obtained for partially occulted and non-occulted flares, respectively. Because part of the flare signal above the background in energy band M2 was imperceptible, the total number of events decreased to 23 and 338, respectively. The central parts of histograms, which contain more than 70% of the events, are shifted one from another. The average value for partially occulted flares is 6.7, and the average value for non-occulted flares is 4.0, while the standard deviations are 1.4 and 1.1, respectively.

The calculation of the $\gamma 3$ index requires the detection of a distinctive signal above the background in energy band H. This once more limits the number of events to 155 non-occulted and only 3 partially occulted flares. In Fig. 5c we therefore present only the normalized histogram for non-occulted flares. The average value is 3.4 and the standard deviation is 0.7. Three partially occulted flares emitting signal strong enough in energy band H show values of the $\gamma 3$ index similar to the typical values obtained for disk flares. They are: event No. 11 650 of 1998 April 23 (Sato 2001; Tomczak 2004), event No. 11 950 of 1998 May 9 (Tomczak 2008), and event No. 26 060 of 2001 April 18 (Hudson et al. 2001). We emphasize that all these events show very spectacular X-ray plasma ejections.

4.2. Deviations from power-law spectra

The histograms of power-law index values in Fig. 5, show a shift towards lower values with increasing photon energies for which the power-law was fitted. This shift is seen for partially occulted as well as non-occulted flares. This appearance is strongly indicative of a contamination of hard X-rays by the emission of thermal plasma, which is expected to decrease with photon energy.

The HXT provides poor spectral resolution (only four broad energy bands), which excludes the reasonable fitting of both a non-thermal power-law component and a thermal one. Therefore, another method for distinguishing between non-thermal and thermal components should be proposed. In this paper, we calculated the average power-law index $\gamma 1$, $\gamma 2$, and $\gamma 3$ for the energy ranges 14–33, 23–53, and 33–93 keV, respectively. If an investigated photon energy spectrum could be described by a single power-law formula, then the obtained values of $\gamma 1$, $\gamma 2$, and $\gamma 3$ should be similar within observational uncertainties. Some larger differences between these values strongly suggest a deviation from the single power-law caused, for example, by the presence of the thermal component.

In Fig. 6, we present the comparison of $\gamma 1$ and $\gamma 2$ for flares presented in the histograms of Fig. 5a,b. For events within the

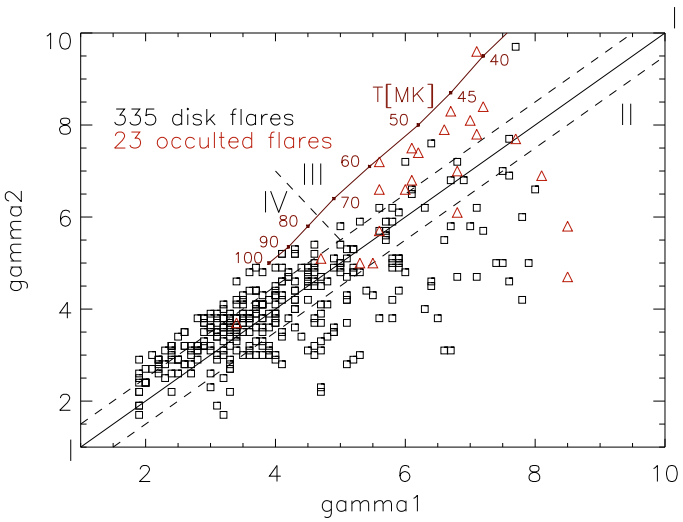

Fig. 6. Comparison between values of the power-law index fitted in two energy ranges: 14–33 keV ($\gamma1$) and 23–53 keV ($\gamma2$). Partially occulted flares are marked with triangles, non-occulted flares are marked with boxes. In dependence on mechanisms responsible for a hard X-ray spectrum formation the points are situated in one of four regions described by digits between I and IV. For additional explanations – see text. Statistics of occurrence is presented in Table 3. The solid narrow line refers to emission of purely thermal plasma with temperatures between 38 and 100 MK.

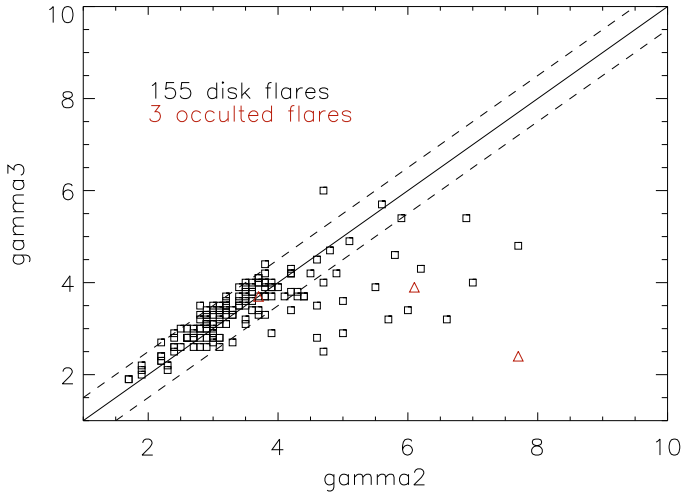

Fig. 7. Comparison between values of the power-law index fitted in two energy ranges: 23–53 keV ($\gamma2$) and 33–93 keV ($\gamma3$). Partially occulted flares are marked with triangles, non occulted flares are marked with boxes. Statistics of occurrence is presented in Table 4. For other explanations – see text.

Table 3. Statistics of different types of spectra in the 14–53 keV energy range.

Area in Fig. 6	Type of spectrum	Partially occulted	Non-occulted
I	non-thermal	30.4%	55.2%
	($\gamma1 \sim \gamma2$)	(7/23)	(185/335)
II	thermal + non-thermal	17.4%	24.2%
	($\gamma1 > \gamma2$)	(4/23)	(81/335)
III	quasi-thermal	52.2%	1.8%
	($\gamma1 < \gamma2$)	(12/23)	(6/335)
IV	albedo	0%	18.8%
	($\gamma1 < \gamma2$)	(0/23)	(63/335)

central region between the two straight dashed lines (area I), differences between $\gamma1$ and $\gamma2$ are below the expected uncertainties, i.e., $|\gamma1 - \gamma2| \leq 0.5$. It means that in the energy range 14–53 keV, their spectra can be described by the single power-law. We consider them as purely non-thermal.

Area II below the central region is occupied by flares for which $(\gamma1 - \gamma2) > 0.5$. It means that their spectra are steeper at lower and flatter at higher energies. We explain this shape as the consequence of the thermal component presence in energy band L.

The area above the central region is occupied by flares for which $(\gamma2 - \gamma1) > 0.5$, which means that their spectra are flatter at lower and steeper at higher energies. This shape suggests a thermal nature. However, purely thermal events should be located in the figure along the solid narrow line above the central region. As we can see, few events are close to this line. The majority of events located in area III is quite quasi-thermal, i.e., the thermal component dominates but is mixed with non-thermal bursts as reported by Tomczak (2001).

Events in area IV are too energetic to explain their spectra by means of thermal emission. Zhang & Huang (2003) proposed that values of $\gamma1$ lower than $\gamma2$ can be caused by Compton backscattering. Known as the photospheric albedo, this effect produces a shift in photon energy from band L to higher energies. Kašparova et al. (2007) demonstrated that the photospheric albedo depends on the heliocentric distance. We checked and found that the longitudes of 38 events out of 50 in area IV, for which Hα coordinates are given in the catalogue, are below 45°. We consider this as being consistent with events situated in area IV having non-thermal spectra modified by the photospheric albedo.

Statistics of the occurrence of flares in different areas of Fig. 6 for partially occulted and non-occulted flares separately is given in Table 3. The results can be summarized as follows. During the hard X-ray maximum in energy band L (14–23 keV), the non-thermal component dominates about 74% of non-occulted flares and only about 30% of partially occulted flares. On the other hand, the thermal component dominates over 50% of partially occulted flares and only about 2% of non-occulted flares.

In Fig. 7, we present the comparison between values of $\gamma2$ and $\gamma3$ for flares from histograms in Fig. 5b,c. The shift in the investigation towards higher energies reduces the heterogeneity of the hard X-ray spectra evident in Fig. 6. The points are concentrated in areas I and II, which means that in the energy range 23–93 keV only pure non-thermal spectra or thermal and non-thermal mixtures frequently occur. The statistical analysis is presented in Table 4. Only total results are given because there are few partially occulted events that show values similar to non-occulted flares. During the hard X-ray maximum in energy band M1 (23–33 keV), about 85% of flares show purely non-thermal spectra, but the thermal component remains in about 15% of events.

We check how deviations from power-law spectra have affected the values of power-law indices. The histograms of the power-law index for flares in area I of Figs. 6 and 7 are presented in Fig. 8. We expect these events to be free of disturbances introduced by the thermal component and the photospheric albedo. The histogram of 185 non-occulted events from Fig. 6 resembles the histogram shown in Fig. 5b. Their medians are 3.7 ± 1.1 and 4.0 ± 1.1, respectively. This small difference is caused by

Table 4. Statistics of different types of spectra in the 23–93 keV energy range

Area in Fig. 7	Type of spectrum	Partially occulted		Non-occulted
I	non-thermal		82.9%	
	($\gamma 2 \sim \gamma 3$)	(1/3)		(130/155)
II	thermal + non-		15.2%	
	thermal ($\gamma 2 > \gamma 3$)	(2/3)		(22/155)
III	quasi-thermal		0%	
	($\gamma 2 < \gamma 3$)	(0/3)		(0/155)
IV	albedo		1.9%	
	($\gamma 2 < \gamma 3$)	(0/3)		(3/155)

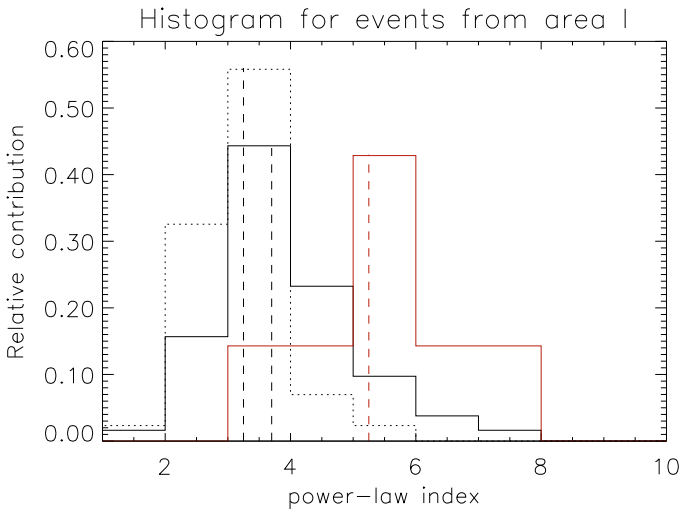

Fig. 8. Normalized histograms of values of the power-law index for flares situated in area I of Figs. 6 and 7 which are believed to be free of disturbances introduced by the thermal component and the photospheric albedo. Solid lines represent the data for energy range 14–53 keV for partially occulted (red) and non-occulted (black) flares separately. The dotted line represents the data for energy range 23–93 keV for non-occulted flares. Medians of histograms are marked with dashed lines.

the small amounts of thermally dominated flares in non-occulted events (see Table 3).

Partially occulted flares represents another case. Because of the frequent occurrence of thermally dominated events (Table 3), the histogram shown in Fig. 8 is clearly shifted towards lower values than the histogram presented in Fig. 5b. The medians are 5.2 ± 1.4 and 6.7 ± 1.4, respectively. In conclusion, after removing the contamination of hard X-rays with emission of thermal plasma, partially occulted flares in our survey exhibit higher values of the power-law index than non-occulted flares. However, the difference between the medians of histograms in Figs. 5b and 8 has decreased from 2.7 to 1.5.

In this way, is it possible to eliminate the contribution of thermal emission completely? The comparison between histograms for non-occulted flares in Fig. 8 for two energy ranges of investigated spectra suggests that the interpretation should be completed with caution. The histogram obtained for higher energies is shifted slightly towards lower values of the power-law index. Its median is 3.2 ± 0.7, i.e., 0.5 lower than the median of the second histogram. This can be interpreted as the cause of a thermal contribution. However, one cannot exclude there being a broken power law with a break energy around 50 keV (i.e., between energy bands M2 and H) and a flatter slope above this value. This situation of an upward "knee" due to the transition from a free-bound to a free-free dominated spectrum was suggested by Brown & Mallik (2008).

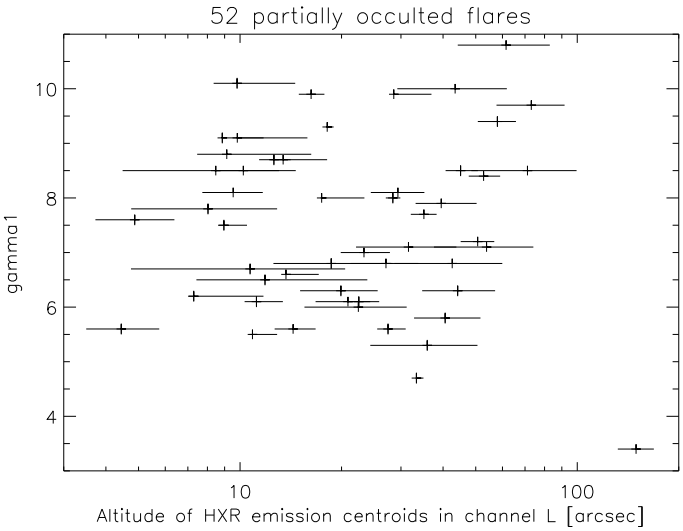

Fig. 9. The power-law index $\gamma 1$ measured between 14–33 keV against the altitude of the centroid of hard X-ray emission imaged in energy band L for 52 partially occulted flares.

4.3. Location of coronal hard X-ray sources

We use the imaging ability of HXT to investigate the spatial structure of the coronal sources. In the first step, we checked the dependence of observed hard X-ray spectra on the altitude of coronal sources above the solar surface.

In Fig. 9, we compared the power-law index $\gamma 1$ to the altitude of the centroid of hard X-ray emission imaged in energy band L for 52 partially occulted flares. In the case of multiple sources, the location of the brightest one was considered. The altitude was the sum of two components of a height above the solar limb h_1 (Col. 9 in Table 2) and a occultation height h_2. The latter one was calculated on the basis of heliospheric coordinates (Col. 6 in Table 2) to be:

$$h_2 = [\sec\theta - 1]\sec\psi R_\odot, \quad (3)$$

where θ is the longitude behind the solar limb and ψ is the latitude. The main source of the altitude error is the uncertainty in the longitude (Col. 7 in Table 2). As we can see, no correlation is observed – flares exhibiting hard X-ray spectra of different shapes occur at each altitude. We also found a lack of correlation between the altitude and the power-law index for higher energy ranges.

How are the non-thermal and thermal components in investigated flares spatially located? To find out, we compared the location of coronal hard X-ray sources to the location of bright loop-top kernels seen in soft X-rays. In Fig. 10, we compared a shift between centroids of emission in these two ranges of X-rays with the altitude of the flares. We considered images of 41 partially occulted flares for which the hard X-ray image in energy band L and the soft X-ray image taken in the Be119 filter were obtained simultaneously. For clarity, error bars are omitted. The typical error in the shift was estimated to be about 2 arcsec. The altitude error is the same as in Fig. 9.

For 26 events (63.4%), the separation between the non-thermal and thermal components is not higher than 5 arcsec. The maximal values of the shift seem to increase with altitude.

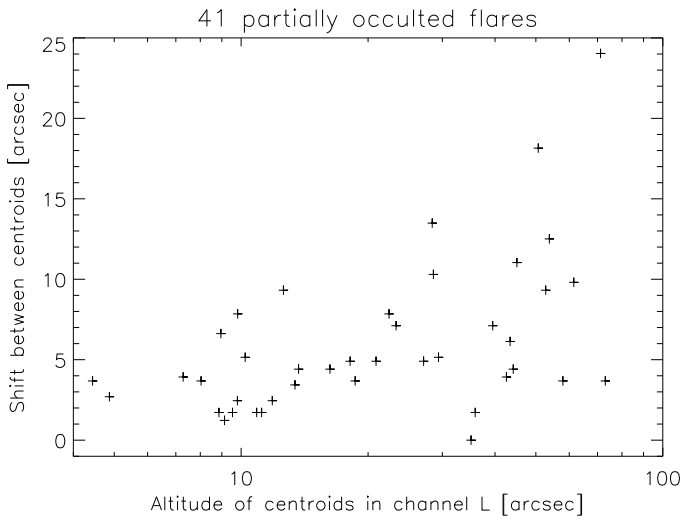

Fig. 10. The shift between centroids of hard (HXT, energy band L) and soft (SXT, Be119 filter) X-ray emission against the altitude of the centroid of hard X-ray emission for 41 partially occulted flares.

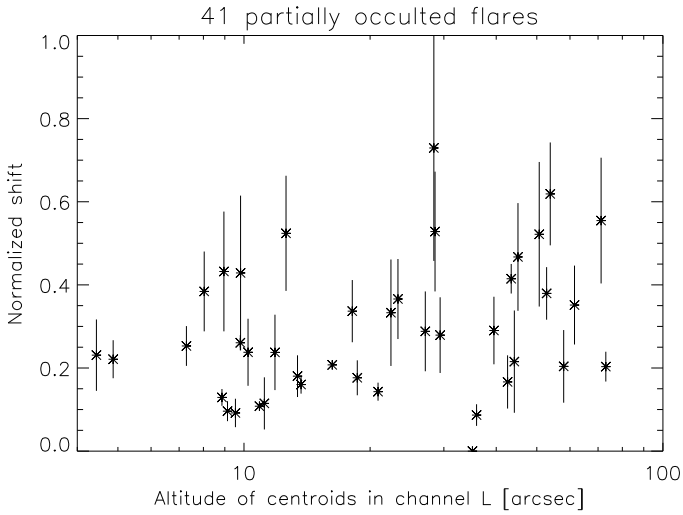

Fig. 11. Shifts from Fig. 10 normalized by dividing with characteristic sizes of hard X-ray sources in energy band L against the altitude of flares for 41 partially occulted flares. For further explanations – see text.

However, this appearance can be caused by an increase with altitude in magnetic features sizes, e.g., soft X-ray loop-top kernels (Preś & Kołomański 2007). To check, we normalized the values presented in Fig. 10 by dividing the shift by the characteristic size of a hard X-ray source.

We calculated the range of values of the normalized shift seen in Fig. 11 as follows. We approximated the hard X-ray sources at the level of $0.5I_{\max}$ as ellipses and divided the shifts from Fig. 10 by the large and small semi-axis of the ellipse. It establishes a lower and higher boundary of the normalized shift, respectively. As we can see, the normalized shift does not depend on altitude, and for the majority of events (36 from 41) does not exceed 0.5. The true cospatiality of hard X-ray and soft X-ray emission for some investigated events is even better because small semi-axes (high boundaries of normalized shifts) were shortened due to an occultation of the solar limb.

Figures 10 and 11 do not distinguish which kind of emission, soft or hard X-ray, is located higher. On the other hand, this appearance is crucial for fitting the data with some theoretical

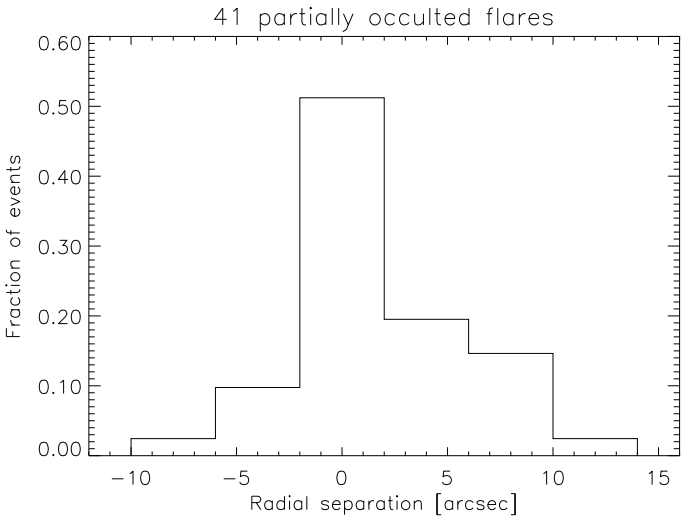

Fig. 12. The radial separation between centroids of hard X-ray and soft X-ray emission for 41 partially occulted flares from Fig. 10. In the most prominent example, the Masuda flare, the radial separation was about 10 arcsec.

models. Therefore, in Fig. 12 we present the radial separation between the centroids of hard X-ray and soft X-ray emission for 41 partially occulted flares from Fig. 10. Almost half of these events (21 from 41) are of the same altitude for both hard X-ay and soft X-ray emission, to within error bars. The second half show differences between them of up to 14 arcsec with a supremacy of events in which hard X-ray emission is located higher than soft X-ray emission (15 from remaining 20). For 5 events, soft X-ray emission was located higher than hard X-ray emission.

In Figs. 9–12, we used images taken in the energy band L as a representation of hard X-ray emission of investigated flares. One may doubt conclusions based on observations in this energy band because of the strong contamination by emission of thermal plasma. Perhaps, Figs. 11 and 12 imply that the hard and soft X-ray emission are cospatial because we observe the same thermal plasma? To verify this idea, we compare the location of the centroids of emission in energy band L to those imaged of higher energies. Unfortunately, a smaller number of events could be checked in this way, because for energy bands M1 and M2, only 16 and 5 images were available, respectively. For only two events, Nos. 11 950 and 25 870, we found that the radial separation between emission in energy band L and at higher energies is greater than 4 arcsec. The remaining 14 events are almost perfectly cospatial.

5. Discussion and interpretation of results

Table 5 collects the results of surveys in which hard X-ray spectra of loop-top sources were investigated and compared to spectra of footpoint sources. The large number of solar flares included in these surveys implies that the results should be statistically important.

Table 5 contains two kinds of data. Papers (1), (2), (4), and (6) described a set of partially occulted flares and presented spectra of coronal hard X-ray sources. Apart from Paper (6), these papers also presented, for a comparison, spectra of non-occulted flares. They are a mixture of emission of loop-top and footpoint sources, although their spectra are understood to be dominated by footpoint sources, especially at higher energies. Based on the imaging spectroscopy, Papers (3) and (5) provide the

Table 5. Surveys comparing power-law spectrum indices of hard X-ray loop-top and footpoint sources.

Satellite	Time period [YY/MM]	Energy range [keV]	Energy res. [keV]	Power-law index γ^a												Refs.[b]
				loop-top						footpoint						
				N	Mn	Md	SD	K	S	N	Mn	Md	SD	K	S	
OSO-7	71/10–72/12	10–300	~30	25	4.8	4.8	1.0	–1.0	0.1	59	3.9	3.8	1.1	–0.6	0.6	(1)
Yohkoh	91/10–96/05	14–33	10	25	8.2	8.1	1.5	–1.1	–0.1	16	7.3	7.7	1.3	–0.9	–0.4	(2)
Yohkoh	91/10–98/08	14–53	10–20	12[c]	6.6	6.2	1.5	0.2	0.4	18[c]	5.2	4.9	1.6	–1.0	0.4	(3)
Yohkoh	91/10–98/08	14–93	10–40	5[c]	5.5	5.3	1.3	–1.5	0.2	13[c]	4.3	4.1	1.0	–1.0	0.7	(3)
Yohkoh	91/10–01/12	14–33	10	52	7.5	7.6	1.6	–0.5	–0.1	620	4.8	4.6	1.6	–0.6	0.4	(4)
Yohkoh	91/10–01/12	23–53	10–20	23	6.7	6.9	1.4	–0.7	–0.2	338	4.0	3.8	1.1	2.1	1.0	(4)
Yohkoh	91/10–01/12	33–93	20–40	3	–	–	–	–	–	155	3.4	3.4	0.7	1.2	0.6	(4)
Yohkoh	91/10-01/12	14–53	10–20	7[d]	5.6	5.2	1.4	–1.3	0.2	185[d]	3.9	3.7	1.1	0.8	0.8	(4)
Yohkoh	91/10–01/12	23–93	10–40	1[d]	–	–	–	–	–	130[d]	3.3	3.2	0.7	1.4	0.6	(4)
RHESSI	02/02-05/07	3–1.7×10^4	1–5	5[c]	5.1	5.6	1.2	–2.0	–0.3	10[c]	2.9	2.8	0.5	–1.4	0.1	(5)
RHESSI	02/02–04/08	3–1.7×10^4	1–5	50	5.4	5.5	1.2	–0.8	0.3	0	–	–	–	–	–	(6)
RHESSI	02/02–05/08	3–1.7×10^4	1–5	0	–	–	–	–	–	174[c]	3.3	3.1	0.5	0.3	0.7	(7)

[a] N – number of events; Mn – mean, Md – median, SD – standard deviation, K – kurtosis; S – skewness.
[b] (1) – Roy & Datlowe (1975); (2) – Mariska & McTiernan (1999); (3) – Petrosian et al. (2002); (4) – this issue; (5) – Battaglia & Benz (2006, 2007); (6) – Krucker & Lin (2008); (7) – Saint-Hilaire et al. (2008).
[c] Imaging spectroscopy.
[d] Events unbiased by the thermal component.

characteristics of the spectra of loop-top and footpoint sources of the same flares. Paper (7) also used the imaging spectroscopy but was limited to footpoint sources.

Histograms of values of the power-law index are represented in Table 5 by routine statistical parameters: mean, median, standard deviation, kurtosis, and skewness. In Papers (1) and (7), the source data were not published, therefore their statistical parameters were calculated based on the assumption that all events in a particular bin equaled to the middle value. The number of events relates to the number of flares or the number of hard X-ray sources in imaging spectroscopy. For *Yohkoh* observations, the energy ranges of spectral fitting are given. In the case of other observations basically, the full available energy coverage were used, in exception to Paper (7) in which the power-law was fitted above the cut-off energy.

The histograms gathered in Table 5 exhibit different shapes for loop-top and footpoint sources. On the other hand, the histograms obtained for the same group of sources show similar shapes. Distributions of spectra of the loop-top sources show basically broad maxima, which are almost symmetrical with a small excess for flatter spectra. Distributions of spectra of the footpoint sources show generally narrower maxima and are strongly asymmetric with an excess for steeper spectra.

To describe the most characteristic values of γ, we use medians, because of the large skewness of distributions, especially for footpoint sources. The broad range of medians within both groups of sources is seen. This wide spread can be caused by many factors such as instrument properties, methods of spectral selection and fitting, or criteria of selection of flares. Nevertheless, all surveys performed have shown that hard X-ray spectra of loop-top sources are systematically steeper than spectra of footpoint sources.

The medians obtained from low-energy bands of the HXT are in particular shifted towards the higher values, due to strong contamination by the thermal component. In Paper (2), very long times of integration additionally favored the influence of the thermal component. To avoid this contamination, it is recommended that we shift the spectral fitting towards higher energies, although this activity limits the number of considered events and attributes the results with a selection effect. The comparison of slopes in different energy ranges of the hard X-ray spectrum, performed in Figs. 6 and 7, allowed us to isolate some flares not produced by the thermal component even at lower energies. Because of this we were able to improve the quality of our statistical analysis and our results look reasonable in comparison with medians obtained from surveys other than *Yohkoh*.

Medians of histograms from Papers (1), (5), (6), and (7) are within the ranges of 4.7–5.5 and 3.1–3.8 for loop-top and footpoint sources, respectively. However, even these values are not completely free of systematic effects. The spectrum of the non-occulted flare is a mixture of photons emitted from both footpoints and the corona. Despite an usual predominance of footpoints, the use of the spectrum of the non-occulted flare as a representation of footpoint sources introduces some bias. On the other hand, imaging spectroscopy can distort spectra of fainter sources (usually the loop-top ones) in the presence of brighter sources (usually the footpoint ones). To overcome this limit, partially occulted flares are chosen, although imprecise selection can be confusing. This was probably true for Paper (1) in which limb flares ($60° < \theta < 90°$) exhibited similar values of γ to those obtained for partially occulted flares. In Paper (6), the distribution at high γ is distorted by observational bias because only flares with hard spectra (above 50 keV) were studied.

We confirmed the presence of a non-thermal component in 11 of the 23 (~48%) partially occulted flares. In 10 of the 23 flares (~43%), some impulsive non-thermal episodes similar to those described by Tomczak (2001) were seen, but the impulses modified the thermal appearance of these flares only slightly. In earlier surveys, the non-thermal component was discovered in 25 of 37 (Roy & Datlowe 1975) and in 50 of 55 flares (Krucker & Lin 2008), i.e., in ~68% and ~91% of events, respectively. We also estimated the frequency of the occurrence of non-thermal components in loop-top sources described by Petrosian et al. (2002), by comparing values of γ in 14–34 and 23–53 keV energy ranges. The result was ~65% (11 of 17 events).

The spatial location of the non-thermal and thermal components is common for the majority of investigated flares. The same rule can be concluded from the earlier papers (Tomczak 2001; Krucker & Lin 2008). Masuda (1994) found that the coronal hard X-ray sources located above the soft X-ray loop-top kernels show spectra that are as flat as the spectra of the footpoint sources. Alexander & Metcalf (1997) obtained a higher

value, $\gamma_{LT} \sim 4$, which implies a distinctly flatter spectrum than for a typical coronal source. In our survey, flares, for which the hard X-ray and soft X-ray components are spatially separated, do not have unusually flat spectra. The extremely shifted event in the survey of Krucker & Lin (2008), i.e., the flare of 2003 November 18, also exhibits a modest value of γ equal to 5.6.

What do the spectra of hard X-ray sources teach us about non-thermal electron beams in solar flares? In the simplest scenario, the same electron beam, described by the power-law index δ, radiates hard X-ray photons in the thin-target loop-top and thick-target footpoint sources. Spectra emitted by these two kinds of sources have indices that differ by 2: $\gamma_{LT} = \delta + 1$ and $\gamma_{FP} = \delta - 1$. Mariska et al. (1996) measured such a difference and presented the interpretation of partially occulted and non-occulted flares, but this small number of investigated events (4 + 4) requires verification by additional data.

Without exception, the surveys presented in Table 5 confirm that the loop-top sources exhibit spectra that are systematically steeper than those of the footpoints, i.e., $\bar{\gamma}_{LT} > \bar{\gamma}_{FP}$. In this paper, we measured the differences between the medians of the distributions of γ values, $\bar{\gamma}_{LT} - \bar{\gamma}_{FP}$, to be about 3. However, the results are affected significantly by contamination from the thermal component. The difference, $\Delta\gamma = \bar{\gamma}_{LT} - \bar{\gamma}_{FP}$, for unaffected events is about 1.5.

The difference, $\Delta\gamma < 2$, means that part of the investigated flares have properties that do not agree with the simplest scenario, $\Delta\gamma = 2$. The shape of the distribution of γ values, which is more symmetric and broader for loop-top sources than footpoint ones, can provide a solution. We guess that some loop-top sources that emitted hard X-rays in the thick-target mechanism are responsible for this. A low-value wing of the γ distribution for loop-top sources is occupied by flares in which X-ray plasma ejections were observed, hence perhaps a kind of magnetic trapping occurs. Another opportunity for coronal thick-target emission may be an unusually-high filling of a flare loop with plasma (Kosugi et al. 1994; Veronig & Brown 2004).

Values of the difference $\Delta\gamma$ higher than 2, obtained by analyses of *RHESSI* observations (Battaglia & Benz 2006, 2007; Krucker & Lin 2008; Saint-Hilaire et al. 2008), require other explanations. For example, separate non-thermal electron beams responsible for loop-top and footpoint sources, deceleration of the precipitating electrons in electric fields due to return currents (Battaglia & Benz 2008), or non-thermal recombination (Brown & Mallik 2008) should be instead be considered.

A lack of correlation between the altitude and the power-law index γ, seen in Fig. 9, suggests that the investigated flares do not respond to the overall (global) magnetic configuration of the solar corona. Their characteristics clearly imply the local magnetic configuration in which these flares were developed.

We identified a non-thermal component in a majority of the investigated flares, in a similar way to the earlier surveys. We have pointed out that in most cases the non-thermal and thermal components (the hard X-ray loop-top source and the bright loop-top kernel, respectively) are cospatial or overlap during the impulsive phase, which confirms that both types of emission come from the common plasma volume and are strongly coupled. Events in which both components are clearly separated, such as a "Masuda flare", seldom occur and are not obviously characterized by a flat hard X-ray spectrum. A similar conclusion was reached by Krucker & Lin (2008).

We emphasize the clear inconsistency between a picture of a flare that is shaped by statistical surveys (i.e., what their typical properties are) and by individual famous events. On the other hand, the models adopted to explain a specific configuration, such as a Masuda flare, are used often as a kind of unification, i.e., explanation of all flares. There is no doubt that their frequency of occurrence should not be a conclusive criterion for performing an interpretation, but there is no reason to recognize such unusual structures, such as a Masuda flare, in each flare, as well.

Why are Masuda-type flares poorly represented in statistical surveys such as ours, even though new examples are more recently reported (Shimizu et al. 2008)? Such an unusual appearance is seen during short episodes occurring randomly in time. On the other hand, one flare is usually represented in catalogues by one time period around the maximum. Thus, it is quite easy to miss such an interesting episode. For example, the famous above-the-loop-top hard X-ray source discovered in a Masuda flare is seen at the beginning of the impulsive phase, and during the hard X-ray maximum it is dominated by the strong footpoint sources. In conclusion, searching for interesting episodes needs careful selection of a sequence of images illustrating the evolution.

6. Interesting groups of events

We provide short descriptions of interesting group of events from our survey.

6.1. Progressive spectral hardening

A relatively less frequent group of flares shows in hard X-rays a progressively hardening spectral evolution that can be described schematically by the pattern "soft-hard-harder" (SHH). These flares are interesting because of their association with other solar activity phenomena such as Coronal Mass Ejections, Solar Energetic Particles, radio bursts type II and type IV. Early reports located the radiation of the SHH flares clearly above the solar surface, inside a postflare loop system where electrons are accelerated and trapped (Cliver et al. 1986, and references therein). However, this picture was directly confirmed only for a few events that occurred some distance behind the solar limb or were imaged below 40 keV by *Hinotori*.

The *Yohkoh* HXT introduced a new picture of SHH flares in which their emission originates close to the solar surface, in flare footpoints (Qiu et al. 2004; Takasaki et al. 2007). The dominance of footpoint emission was also confirmed for some SHH flares observed by *RHESSI* (Saldanha et al. 2008; Grigis & Benz 2008). Thick-target footpoint sources primarily emit their hard X-rays immediately, and the SHH spectral pattern cannot therefore be explained by the trapping mechanism alone. Footpoint SHH flares strongly imply a physical mechanism that continuously accelerates electrons to ever higher energies is involved.

In our survey, we have found three flares exhibiting the SHH spectral pattern. Their basic characteristics are given in Table 6. All occurred far enough behind the solar limb to eliminate the hard X-ray emission from footpoints, and because of this, closer insight into the corona was possible. Tomczak (2008) noted that the SHH spectral pattern coincides in time with the occurrence of a new coronal source. In the case of 1998 May 9, this source moved away gradually, its velocity increasing from 25 to 80 km s^{-1}.

The progressive spectral hardening in flares from Table 6 was always preceded by a phase of the "soft-hard-harder" (SHH) spectral evolution pattern in which another hard X-ray source was seen. This behavior strongly suggests that a switch between the SHS and SHH spectral pattern required significant reconfiguration of the magnetic structure of a flare.

Table 6. List of flares showing progressive spectral hardening.

Catalogue number	Date	GOES class	Longitude	Occultation height [Mm]	γ range	Time interval
9700	1994 February 27	M2.8	W97.5	6.1	6→4	09:09–09:18
11950	1998 May 9	M7.7	W102.3	17.1	6.0→3.4	03:29–03:39
25540[a]	2001 April 1	M5.5	E107.0	34.1	>11→7.6[b]	11:48-11:54

[a] Only the decay phase is available.
[b] Strong contamination with emission of thermal plasma.

Table 7. List of *Yohkoh* coronal γ-ray flares.

Catalogue number	Date	GOES class	Longitude	Occultation height [Mm]	Photons energy [keV]
6240	1992 November 2	X9.0	W97.9	7.4	<600[a]
11650	1998 April 23	X1.2	E103.7	21.4	<250
11950	1998 May 9	M7.7	W102.3	17.1	<200
13650	1998 November 24	X1.0	W103.1	21.5	<600[a]
26060	2001 April 18	C2.2	W116.9	90.5	<250

[a] Only the decay phase is available.

6.2. Coronal γ-ray sources

Because of the RHESSI imaging capabilities it is possible to obtain hard X-ray images at higher energies than possible before. The results, which are limited by counting statistics and dynamic range, show that γ-rays are usually emitted from footpoints (Saldanha et al. 2008), although an example of the coronal source is also known (Krucker et al. 2008b). *Yohkoh* could not image at such high energies, although in the HXT Flare Catalogue we found five events, recorded by the WBS, that occurred behind the solar limb and for which spectra reach at least 200 keV (see Table 7).

All these events occurred far enough behind the solar limb to be certain that the high-energy photons are emitted from the corona. In this way, without imaging, we obtain an independent confirmation that γ-rays can be produced in the corona. The flare of 1998 November 24, which produced 600-keV photons about 3 minutes after its maximum, attracted special attention. According to the CGRO/BATSE light curve, the flux decreased almost twice during this time interval, hence photons more energetic than 600 keV at most were emitted.

Krucker et al. (2008b) interpreted the coronal γ-ray emission as relativistic electron-electron bremsstrahlung at energies perhaps of a few MeV. Therefore, these observations directly imply that flare-accelerated MeV electrons reside stably in the corona, losing their energy collisionally and producing γ-ray continuum.

7. Conclusions

Among the 1286 flares detected in the *Yohkoh* Hard X-ray Telescope Flare Catalogue, for which hard X-ray images had been enclosed, we identified 98 events that occurred behind the solar limb. The obscurity of footpoints, which are usually brighter in hard X-rays, allowed us to isolate the coronal parts of these flares for a more detailed analysis. We investigated hard X-ray spectra and the spatial structure of partially occulted flares. In most cases, we found that their hard X-ray spectra consists of two cospatial components, non-thermal and thermal.

We note that the spectra of partially occulted flares are systematically steeper than spectra of non-occulted events in the catalogue. This shows that the hard X-ray emission in solar flares is usually less energetic in the corona (loop-top sources) than close to the solar surface (footpoint sources). The difference between the median values of the power-law index for both classes of sources, $\Delta\gamma = \bar{\gamma}_{\rm LT} - \bar{\gamma}_{\rm FP}$, is about 3. However, this result is strongly affected by thermal emission. For events unbiased by the thermal component, the difference $\Delta\gamma$ equals 1.5. The value obtained is similar to the results of other surveys.

We conclude that the different slopes of the non-thermal component are basically caused by different emission mechanisms: thin-target for loop-top sources and thick-target for footpoint sources. The difference of $\Delta\gamma$, which is smaller than 2, suggests that exceptions to this rule exist. We have presented arguments that part of coronal hard X-ray sources is a thick-target instead of a thin-target, e.g., several unusually high-energetic events that occurred in the configuration indicative of magnetic trapping. An additional argument that flare characteristics are dependent on the local magnetic configuration in which they develop, reflects a lack of correlation between the altitude of flares and the hard X-ray power-law index γ.

Additional high-quality observations and high-precision analyses are needed to derive further details about non-thermal electron acceleration and propagation in solar flares. Detailed imaging spectroscopy of individual events as well as massive surveys of many flares are desired.

Acknowledgements. The *Yohkoh* satellite is a project of the Institute of Space and Astronautical Science of Japan. I am grateful to late Professor Takeo Kosugi, Dr. Jun Sato, and their collaborators for preparing the *Yohkoh* HXT Flare Catalogue which made this work easier. I thank also my colleagues from a working group of the International Space Science Institute (Bern, Switzerland), dedicated to coronal hard X-ray sources, for a fruitful discussion. I appreciate valuable remarks of referee, Dr. S. Krucker, which helped to improve this paper. This work was supported by Polish Ministry of Science and High Education grant No. N N203 1937 33.

References

Alexander, D., & Metcalf, T. R. 1997, ApJ, 456, 751
Battaglia, M., & Benz, A. O. 2006, A&A, 456, 751
Battaglia, M., & Benz, A. O. 2007, A&A, 466, 713
Battaglia, M., & Benz, A. O. 2008, A&A, 487, 337
Brown, J. C. 1971, Sol. Phys., 18, 489
Brown, J. C., & Mallik, P. C. V. 2008, A&A, 481, 507

Catalano, C. P., & Van Allen, J. A. 1973, ApJ, 185, 335
Cliver, E. W., Dennis, B. R., Kiplinger, A. L., et al. 1986, ApJ, 305, 920
Frost, K. J., & Dennis, B. R. 1971, ApJ, 165, 655
Grigis, P. C., & Benz, A. O. 2008, ApJ, 683, 1180
Hudson, H. S. 1978, ApJ, 224, 235
Hudson, H. S., Lin, R. P., & Stewart, R. T. 1982, Sol. Phys., 75, 245
Hudson, H. S., Strong, K. T., Dennis, B. R., et al. 1994, ApJ, 422, L25
Hudson, H. S., Kosugi, T., Nitta, N. V., & Shimojo, M. 2001, ApJ, 561, L211
Kane, S. R., Fenimore, E. E., Klebesadel, R. W., & Laros, R. G. 1982, ApJ, 254, L53
Kašparova, J., Kontar, E. P., & Brown, J. C. 2007, A&A, 466, 705
Khan, J. I., Harra-Murnion, L. K., Hudson, H. S., Lemen, J. R., & Sterling, A. C. 1995, ApJ, 452, L153
Kosugi, T., Makishima, K., Murakami, T., et al. 1991, Sol. Phys., 136, 17
Kosugi, T., & Yohkoh HXT Group 1993, The *Yohkoh* HXT Databook (I), 1991 October–1992 December, National Astronomical Observatory, Mitaka, Tokyo, Japan (Version 1)
Kosugi, T., Sakao, T., Masuda, S., et al. 1994, Proc. Kofu Symposium: New Look at the Sun with Emphasis on Advanced Observations of Coronal Dynamics and Flares, ed. S. Enome, & T. Hirayama, Nobeyama Radio Observatory Report No. 360, 127
Kosugi, T., Sawa, M., Sakao, T., et al. 1995, The Yohkoh HXT Databook: October 1991–December 1994, National Astronomical Observatory, Mitaka, Tokyo, Japan (Version 2)
Krucker, S., & Lin, R. P. 2008, ApJ, 673, 1181
Krucker, S., White, S. M., & Lin, R. P. 2007a, ApJ, 669, L49
Krucker, S., Hannah, I. G., & Lin, R. P. 2007b, ApJ, 671, L193
Krucker, S., Battaglia, M., Cargill, P. J., et al. 2008a, A&ARv, 16, 155
Krucker, S., Hurford, G. J., McKinnon, A. L., Shih, A. Y., & Lin, R. P. 2008b, ApJ, 678, L63
Krucker, S., Hudson, H. S., White, S. M., Wuelser, J.-P., & Lin, R. P. 2009, in preparation
Li, Y. P., & Gan, W. Q. 2006, ApJ, 652, L61
Li, Y. P., & Gan, W. Q. 2007, Adv. Space Res., 39, 1389
Lin, R. P. 1974, Space Sci. Rev., 16, 189
Liu, W., Petrosian, V., Dennis, B. R., & Jiang, Y. W. 2008, ApJ, 676, 704
Mariska, J. T., & Doschek, G. A. 1997, ApJ, 485, 904
Mariska, J. T., & McTiernan, J. M. 1999, ApJ, 514, 484
Mariska, J. T., Sakao, T., & Bentley, R. D. 1996, ApJ, 459, 815
Masuda, S. 1994, Ph.D. Thesis, University of Tokyo
Masuda S., Kosugi, T., Hara, H., Tsuneta, S., & Ogawara, Y. 1994, Nature, 371, 495
McKenzie, D. L. 1975, Sol. Phys., 40, 183
Newton, H. W., & Nunn, M. L. 1951, MNRAS, 111, 413
Ohyama, M., & Shibata, K. 1997, PASJ, 49, 249
Petrosian, V., Donaghy, T. Q., & McTiernan, J. M. 2002, ApJ, 569, 459
Preś, P., & Kołomański, S. 2007, Cent. Eur. Astrophys. Bull., 31, 87
Qiu, J., Lee, J., & Gary, D. E. 2004, ApJ, 603, 335
Roy, J.-R., & Datlowe, D. W. 1975, Sol. Phys., 40, 165
Sato, J. 2001, ApJ, 558, L137
Sato, J., Sawa, M., Masuda, S., et al. 1998, The Yohkoh HXT Image Catalogue: October 1991–August 1998, Nobeyama Radio Observatory, National Astronomical Observatory, Japan (Version 3)
Sato, J., Sawa, M., Yoshimura, K., Masuda, S., & Kosugi, T. 2003, The *Yohkoh* HXT/SXT Flare Catalogue, Montana State University and Institute of Space and Astronautical Science (Version 4)
Sato, J., Matsumoto, Y., Yoshimura, K., et al. 2006, Sol. Phys., 236, 351 (Version 5)
Saint-Hilaire, P., Krucker, S., & Lin, R. P. 2008, Sol. Phys., 250, 53
Saldanha, R., Krucker, S., & Lin, R. P. 2008 ApJ, 673, 1169
Shimizu, M., Nishida, K., Takasaki, H., et. al. 2008, ApJ, 683, L203
Sterling, A. C., Harra-Murnion, L. K., Hudson, H. S., & Lemen, J. R. 1996, ApJ, 464, 498
Takasaki, H., Kiyohara, J., Asai, A., et al. 2007, ApJ, 661, 1234
Tomczak, M. 1997, A&A, 317, 223
Tomczak, M. 2001, A&A, 366, 294
Tomczak, M. 2004, A&A, 417, 1133
Tomczak, M. 2005, Adv. Space Res., 35, 1732
Tomczak, M. 2008, Cent. Eur. Astrophys. Bull., 32, 59
Tomczak, M., & Ciborski, T. 2007, A&A, 461, 315
Veronig, A. M., & Brown, J. C. 2004, ApJ, 603, L117
Ward, F. 1966, ApJ, 145, 416
Zhang, J., & Huang, G. L. 2003, ApJ, 592, L49
Zirin, H., Ingham, W., Hudson, H., & McKenzie, D. 1969, Sol. Phys., 9, 269